

Chapter 7

An Atomic-Scale Perspective of the Challenging Microstructure of $\text{YBa}_2\text{Cu}_3\text{O}_{7-x}$ Thin Films



**Bernat Mundet, Roger Guzmán, Elena Bartolomé, Andrew R. Lupini,
Steven Hartman, Rohan Mishra, and Jaume Gázquez**

7.1 Introduction

The advent of high-temperature superconductivity has opened up a new frontier in advanced power systems and high-field magnets. However, in the early days, achieving high current densities in high-temperature superconductor (HTS) wires was a fundamental problem. This was attributed to grain boundaries that act as weak

B. Mundet · R. Guzmán · J. Gázquez (✉)

Department of Superconductivity, Institut de Ciència de Materials de Barcelona (ICMAB-CSIC),
Barcelona, Spain

e-mail: bmundet@icmab.es; rguzman@icmab.es; jgazqueza@gmail.com

E. Bartolomé

Escola Universitària Salesiana de Sarrià (EUSS), Barcelona, Spain

e-mail: ebartolome@euss.es

A. R. Lupini

Institute for Functional Imaging of Materials Oak Ridge National Laboratory, Oak Ridge, TN,
USA

Materials Sciences and Technology Division Oak Ridge National Laboratory, Oak Ridge, TN,
USA

e-mail: arl1000@ornl.gov

S. Hartman

Institute of Materials Science and Engineering, Washington University in St. Louis, St. Louis,
MO, USA

e-mail: steven.t.hartman@wustl.edu

R. Mishra

Institute of Materials Science and Engineering, Washington University in St. Louis, St. Louis,
MO, USA

Department of Mechanical Engineering and Materials Science, Washington University
in St. Louis, St. Louis, MO, USA

e-mail: rmishra@wustl.edu

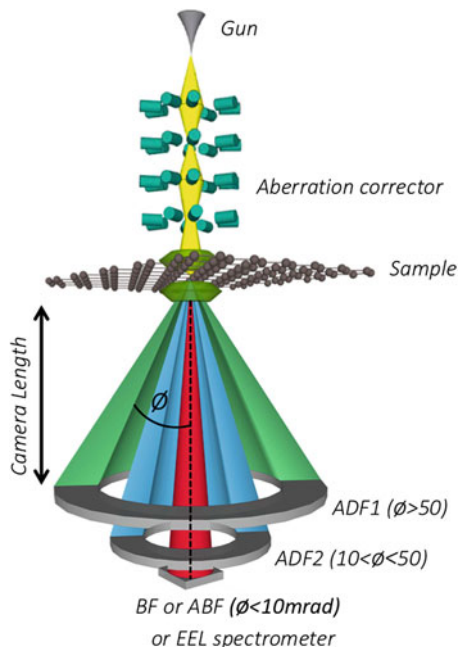
links in these materials by drastically limiting the current flow. The work of Dimos, Chaudhari, and Mannhart [1] provided a breakthrough to solve this grain boundary problem; by measuring the critical current of $\text{YBa}_2\text{Cu}_3\text{O}_{7-x}$ (YBCO) thin films deposited epitaxially on bicrystal substrates, which enabled control over the misorientation of grain boundaries in YBCO, they found that the critical-current density J_c across the grain boundary falls exponentially on increasing the misorientation angle of the grain boundaries. Their results suggested an alternative path to achieve long wires with high J_c : texturing the HTS material biaxially so as to limit the misorientation angle between adjacent grains to only a few degrees. This led to the second generation (2G) of HTS wires, also called coated conductors, with promise for bulk power transmission and magnet applications [2]. Nowadays, the epitaxial thin film structure of these materials allows generation of record critical-current densities observed so far in many high-temperature superconductors. Nevertheless, critical-current densities, and therefore power applications, can be tremendously boosted if nanostructured conductors with artificial pinning centers immobilizing quantized vortices at high-temperature and magnetic fields are produced. To date, all the proposed strategies for the preparation of nanostructured YBCO films involves the use of a secondary non-superconducting phase [3–8] either to use its normal-state volume or to generate defects within the matrix of YBCO that act as localization centers for vortices, which are quanta of magnetic flux [9–16].

The strategies to induce vortex pinning consist of creating non-superconducting regions—any defect that may break the crystallinity of the YBCO matrix—which will oppose the movement of vortices. If the Lorentz force, $\mathbf{J} \times \mathbf{B}$, on a vortex exceeds the pinning force induced by a defect, the magnetic flux lines move and generate resistive losses, thus limiting the critical current. Hence, achieving efficient vortex pinning is crucial for the application of superconductors as loss-free conductors in cables and in magnetic coils.

Furthermore, due to the very small coherence length ξ of YBCO ($\xi_{ab} \approx 2$ nm, $\xi_c \approx 0.4$ nm), the range of defects that can pin vortices is vast: point-defect clusters, dislocations, stacking faults, anti-phase boundaries, grain boundaries, voids, and secondary phases. However, the localization of the vortices' core at these insulating regions is not the only effective vortex-pinning mechanism. Recent results have pointed out the possibility that the formation of Cooper pairs might be quenched under tensile strain, thereby, enabling another strategy to pin vortices in high-temperature superconductors [17, 18].

Although YBCO has been long studied, the use of improved characterization techniques has shed light on the complex defect landscape of YBCO thin films and nanocomposites and unveiled the presence of previously disregarded defects embedded in YBCO with peculiar electronic and magnetic properties. All the defects shown herein may be found in any YBCO thin film, regardless of the deposition and growth method used to fabricate it. We will pay attention to the atomic structure of individual defects, the complexity of which can be shown in real space and with atomic resolution using aberration-corrected scanning transmission electron microscopy (STEM).

Fig. 7.1 Simplified schematic of an aberration-corrected STEM. The electrons are accelerated in the gun; condenser lenses are used to adjust the beam current and beam coherence and to couple to the aberration corrector. The objective lens focuses the probe, which is scanned across the sample by the scan coils. The Annular Dark Field detector 1 (ADF1) and 2 (ADF2) collect electrons scattered to high and low angles, respectively. The removable Bright Field or Annular Bright Field Detectors (ABF) are located at the center of the microscope column, as well as the electron energy loss spectrometer (EELS)



The implementation of spherical aberration correctors in modern electron microscopes has pushed their spatial resolution into the sub-Ångstrom regime and their sensitivity for imaging and spectroscopy of both light and heavy elements. In an aberration-corrected STEM, a schematic of which is shown in Fig. 7.1, an electron probe is focused to a spot size of ~ 1 Å and rastered over a very thin sample (5–100 nm thick). The scattered electrons are then collected to form the image as a function of the probe position over the sample. In addition, the use of post-specimen lenses and multiple detectors allows the simultaneous collection of electrons that are scattered to different angles, enabling the detection of complementary signals. Probably the main benefit of the STEM configuration is that it is possible to obtain the so-called Z-contrast image—with Z being the atomic number—which is formed by collecting the electrons scattered out to high angles by placing a high-angle annular dark field (HAADF) detector, ADF1 in Fig. 7.1. In this imaging mode, the brightness associated to each atomic column is approximately proportional to its Z^2 number [19–21]. This imaging mode has two main advantages, the first is that the resulting images are incoherent, which makes the simulation of the imaged structure unnecessary and therefore the interpretation of the image straightforward [22]. The second advantage is the possibility to form an image of point defects, as it is going to be shown in this chapter. The wider probe-forming aperture available after aberration correction gives a reduced depth of focus, making it possible to optically section through a sample in a way similar to confocal optical microscopy [23].

As mentioned above, all the transmitted electrons in an STEM can be gathered with different detectors, see Fig. 7.1, each one providing complementary information, either as an image, if another imaging detector is used, or as a spectra, with an electron energy loss spectrometer, which collects those electrons that have lost some energy as a result of inelastic scattering from the sample, which are typically deviated to low angles. Hence, we have combined High-Angle Annular Dark Field (HAADF), Low-Angle Annular Dark Field (LAADF), and Annular Bright Field (ABF) imaging modes with Electron Energy Loss Spectroscopy (EELS) in an STEM, and complemented with X-Ray absorption spectroscopy (XAS), X-Ray magnetic circular dichroism (XMCD), and density-functional-theory calculations (DFT) to probe the atomic structure, the chemistry, the magnetic and the electronic structure of the defects found in YBCO thin films.

7.2 The Structure of YBCO

To optimize superconductivity in cuprates, and YBCO in particular, several structural features are needed, resulting in a rather complex chemistry. First, copper oxide planes are essential. These have a stoichiometry of CuO_2 and form a corner-connected square-pyramidal plane (gray arrows in Fig. 7.2a). Hence, cuprates are described as *layered perovskites*. YBCO has two hole-doped CuO_2 planes separated by Y cations without allowing intercalation of O between Cu's in adjacent planes.

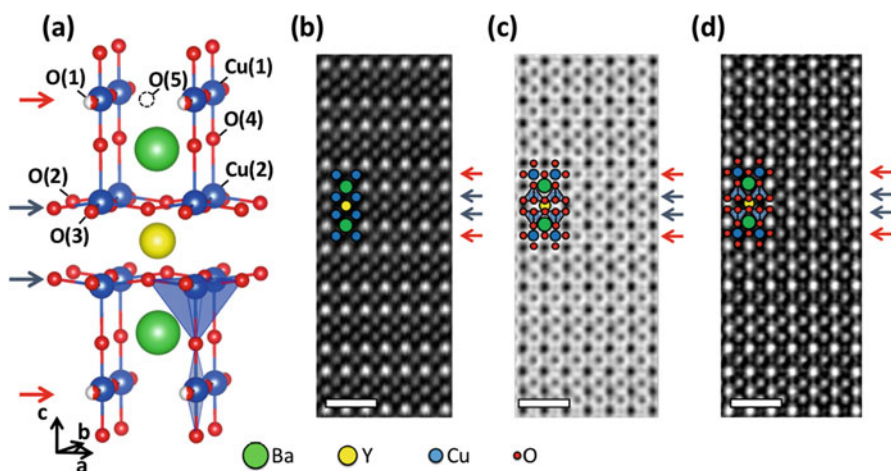


Fig. 7.2 (a) Sketch of the orthorhombic YBCO unit cell. (b) Z-contrast, (c) ABF, and (d) contrast-inverted ABF images, showing the YBCO crystal structure viewed along the $[100]$ zone-axis direction. Scale bars: 1 nm. Ba, Y, Cu, and O are represented with green, yellow, blue, and red circles, respectively. The blue and red arrows signal two superconducting CuO_2 planes and two CuO chains, respectively. Data acquired at 300 kV on the aberration-corrected FEI Titan

A larger cation, Ba supports apical coordination of a further oxygen to copper, and provides connection to an additional CuO_x layer, also referred to as Cu-O chains. These CuO_x layers are termed as a “charge reservoir” as they compensate for the hole-doping of the CuO_2 planes. In the orthorhombic phase, the Cu-O chains align along the b axis and the oxygen occupies the so-called O(1) site, whereas the sites on the a axis [O(5)] are empty.

Figure 7.2b shows a high-resolution Z -contrast image where the YBCO structure is viewed along the [100] zone-axis orientation. As the brightness associated to each atomic column is roughly proportional to its Z^2 number, it allows distinguishing all the heavy atomic species in the structure, the Ba, Y, and Cu cations. In addition, one can simultaneously gather the electrons of the direct beam using an ABF detector, which discards the central part of the bright field disk. Such a detector enables us to visualize atomic columns composed of light atoms [24]. The ABF image displayed in Fig. 7.2c and its inverse-contrast image in Fig. 7.2d reveals the oxygen sub-lattice of YBCO. All O atoms belonging to the superconducting planes (blue arrows) are not confined at the same basal plane as the Cu atoms that they are bonded to. They are slightly shifted towards the Y cation, resulting in a rippling pattern with the Cu atoms when moving along the basal direction, see Fig. 7.2d.

From the electronic point of view, undoped YBCO (if one lowers the O content to 6) becomes insulating and contains Cu^{2+} (d^9 configuration) within the CuO_2 sheets. The uppermost $3d$ orbital is $3d_{x^2-y^2}$ and is singly occupied. This lone electron is localized on Cu due to strong Coulomb repulsion and aligned antiferromagnetically on the CuO_2 plane. In the remaining Cu chains, the Cu^{1+} ion has a closed-shell configuration (d^{10}) and is insulating. The addition of O in YBCO introduces trivalent Cu in the CuO_2 planes, being divalent in the Cu-O chains. The holes are transferred between them through the apical O(2) of the Ba-O plane [25]. Further hole-doping increases T_c , which reaches its maximum at a O content of about 6.92 [26].

Thanks to the particular geometry of the STEM, one can characterize the electronic structure of a compound with atomic resolution using EEL spectroscopy [19], which gives information about the energy that the transmitted electrons lose when they interact with the core electrons of the crystal, providing information of the electronic energy states that remain empty being above the Fermi energy. In perovskites, the O $2p$ - and transition metal $3d$ -states are strongly hybridized, as they have similar energies and lay close to the Fermi level, which helps to probe the metal-oxygen bond. In particular, the combination of STEM and EELS allows for measuring the O-K and Cu-L edges with sufficient spatial and energy resolution to distinguish the role of the superconducting planes and chains in real space, see Fig. 7.3a. Following the dipole-selection rules, the O-K near-edge structure arises from the excitations of the O $1s$ -electrons to the O $2p$ -states, whereas the Cu-L edge results from the excitation of the $2p$ -electrons into the empty $3d$ -states. Thus, any change in the electronic structure can be probed by studying the variations in the fine structure of both edges. For instance, the onset of the O-K edge pre-peak is observed to shift to higher energies when lowering the O content within the YBCO structure [27, 28].

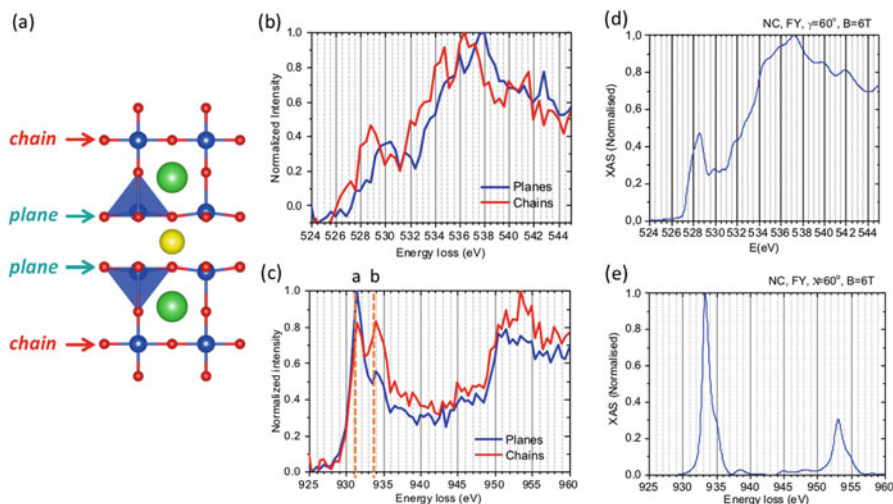


Fig. 7.3 (a) The crystal structure of the orthorhombic YBCO unit cell with arrows to show the Cu-O chain and the CuO₂ plane from which the EEL spectra in (b) and (c) were acquired. (b) Site-specific O-K edges associated to the chain (in red) and superconducting plane (in blue). (c) Site-specific Cu-L edges associated to the chain (in red) and superconducting plane (in blue). Data acquired at 100 kV on the aberration-corrected Nion UltraSTEM. (d, e) O-K and Cu-L XAS spectra. All spectra were obtained from a YBCO nanocomposite with Ba₂YTaO₆ nanoparticles

Figure 7.3b, c show the O-K and the Cu-L edges from the superconducting planes (in blue) and from the chains (in red), respectively. Both edges have been acquired from a YBCO nanocomposite thin film and are compared with the macroscopic and averaged X-ray absorption spectroscopy (XAS) data in Fig. 7.3d, e, respectively. One can clearly resolve significant differences between the O-K and Cu-L spectra in the chains and in the planes. Regarding the O-K edge, the most obvious is the difference in energy of the onset of the O-K pre-peak, which is found at 527 eV in the chains and at 528.5 eV in the planes, and their intensity, which is lower in the planes. In addition, the central peak, located in the 534–540 eV range, is also shifted to a higher energy in the planes.

The Cu-L edge fine structure also reveals differences between CuO₂ planes and Cu-O chains see Fig. 7.3c. At the chains, the L_3 peak splits into the *a* and *b* peaks, centered at 931.5 eV and 934 eV, respectively. A chemical shift towards higher energies is observed in the Cu-L edge when the Cu oxidation state is reduced [29, 30]. Peak *a* is associated to a Cu oxidation state of (+2) whereas peak *b* is associated to (+1). Therefore, the splitting of the L_3 peak suggests that a mixture of Cu+1/+2 cations is present within the single-chain layers. On the other hand, the L_3 peak associated to the superconducting Cu atoms is mainly composed by peak *a*, as it has an oxidation state of Cu⁺². The O-K and Cu-L edges spectra shown here for a nanocomposite film match extremely well with those obtained from a YBCO single crystal [28], and prove that aberration correction STEM is able to image the real-

space electronic structure in the planes and chains of YBCO thin films. This kind of characterization may help understanding the changes in the electronic structure with defects in YBCO with atomic resolution.

7.3 The Microstructure of YBCO Thin Films

Efficient and viable superconducting films require a fine balance between defects at both nanoscale and mesoscale levels. As stated above, both YBCO lattice defects and non-superconducting nanostructures can effectively pin the magnetic flux, thus enabling high J_c under external applied magnetic fields. Indeed, one of the most effective ways to enhance the physical properties of YBCO thin films is to introduce secondary phase nanoparticles within the YBCO film. Barium perovskite nanoinclusions BaMO_3 ($M = \text{Zr, Hf, Sn}$), double perovskites $\text{Ba}_2\text{RETaO}_6$ ($\text{RE} = \text{Y, Gd, Er}$) and binary rare earth oxides RE_2O_3 ($\text{RE} = \text{Y, Dy, Ho}$) have been successfully incorporated to YBCO epitaxial matrix by different deposition techniques leading to nanocomposite films with improved flux-pinning properties [6–8, 18, 31–39]. However, one must consider that the embedded nanostructures reduce the current-carrying cross section; therefore, the density, distribution, and separation among the pinning centers are also critical to establish a balance between flux-pinning and current-blocking. Understanding the influence of the nanoinclusions on the YBCO texture and microstructure is thus essential for correlating the structure with its superconducting properties.

The best way to visualize the complexity of a YBCO nanocomposite thin film microstructure is by using an aberration-corrected STEM. Figure 7.4a, b shows two low-magnification STEM images, acquired simultaneously, of a solution-based YBCO nanocomposite with Ba_2YTaO_6 (BYTO) nanoparticles embedded within the YBCO matrix [40]. The different contrast of these images is the result of using different acquisition modes. Figure 7.3a is a traditional HAADF image, in which the contrast ensues only from high-angle scattering of electrons. On the other hand, the image in Fig. 7.4b is the result of collecting electrons scattered to lower angles (LA). This LAADF imaging mode allows one to image contrast related to defects, i.e., deformations of the atomic columns that lead to a dechanneling of the incident electron beam [41, 42]. HAADF or Z-contrast STEM imaging is ideal for describing and identifying defects in such a highly distorted YBCO matrix, as resulting incoherent images provide almost direct interpretation; they do not suffer from contrast reversal due to the strong dependence on thickness and defocus in conventional phase-contrast TEM imaging [21]. At the same time, LAADF imaging allows for detecting the strain fields along defects and the distortions associated to them.

These images show that, apart from the secondary phases embedded within the superconductor matrix, the $\text{YBa}_2\text{Cu}_4\text{O}_7$ (Y124) intergrowth is the most common and most widespread structural defect in YBCO nanocomposite films, which shares, basically, the same structure as YBCO with the addition of a second CuO_x layer,

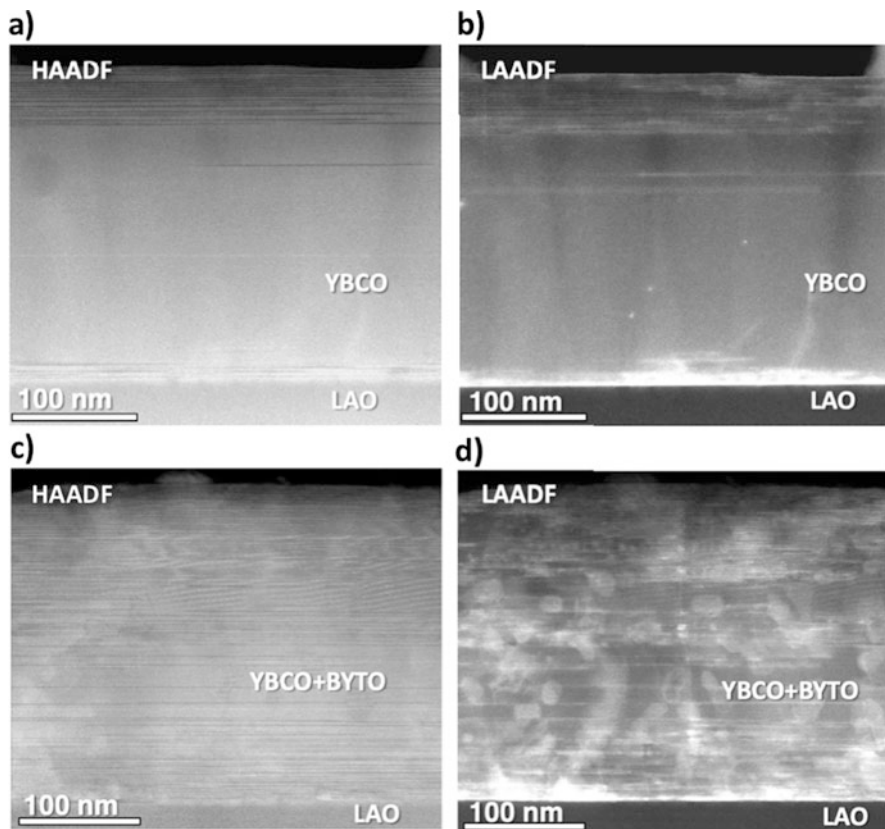


Fig. 7.4 Comparison between the microstructure of a pristine YBCO film and a YBCO-6% BYTO nanocomposite film. (a, b) and (c, d) are simultaneously acquired HAADF and LAADF low-magnification images, respectively. Data acquired at 300 kV on the aberration-corrected FEI Titan. Adapted from [13]

instead of one [43, 44], as shown in Fig. 7.5. Comparing the HAADF and LAADF images, one can realize that the introduction of secondary phase nanoparticles within the YBCO layer dramatically increases the number of these planar defects, which appear as dark stripes in the HAADF imaging mode and brighter in LAADF images. In addition, due to the presence of BYTO nanoparticles and the numerous intergrowths, the focus is lost in several parts of the image, revealing a highly distorted YBCO matrix, which accounts for strain-induced contrast as observed in the LAADF image in Fig. 7.4d.

The presence of an extra CuO chain in the YBCO lattice introduces a 1.9 Å increase along the c -axis and a non-conservative stacking fault with a displacement vector of $[0, b/2, c/6]$ [44], which shifts the two parts of the structure on either side of the fault laterally by $1/2 b$ when viewed along the $[100]$ direction, as shown in Fig. 7.5a, b. Accordingly, the Cu atoms in this double Cu-O chains have a triangle-

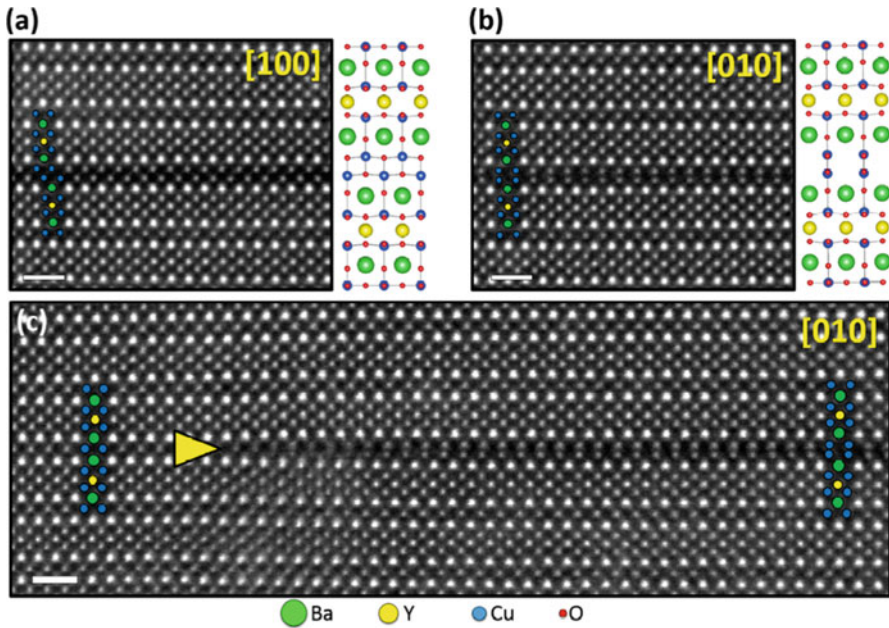


Fig. 7.5 High-resolution Z-contrast images of an isolated Y124 intergrowth embedded within the YBCO crystal structure, which are viewed along either the (a) [100] or, (b) and (c) [010] zone-axis directions. The edge of this planar defect, composed by a partial dislocation, is viewed in (c) (yellow arrow). The YBCO structure is sketched with green (Ba), yellow (Y), and blue (Cu) circles. Scale bars: 1 nm. Image acquired at 300 kV on the aberration-corrected FEI Titan

shaped atomic arrangement when viewed along the [100] zone axis, while they lay head-to-head when viewed along the [010] zone axis. When this double Cu-O chain occurs as a single layer with a finite lateral extent, it is structurally analogous to a Frank loop dislocation, i.e., an extrinsic stacking fault surrounded by a partial dislocation, see Fig. 7.5c.

The genesis of the Y124 intergrowths—which appear not only in YBCO nanocomposites but in all YBCO thin films, regardless of the growth method used—is expected to be linked to stress-related effects and stems from the fundamental crystal structure of YBCO superconductors, which have a marked two-dimensional behavior, which in turn determines their structural anisotropy and superconducting properties. Such anisotropy also affects the evolution of crystallographic defects, hindering the creation of correlated defects perpendicular to the superconducting CuO_2 planes. A common way to dissipate this strain energy is through the generation and growth of dislocations. However, dislocations in YBCO mostly belong to the glide systems $[100](001)$, $[010](001)$, and $\langle 110 \rangle (001)$, i.e., they are confined to the basal plane [45]. Given the large lattice parameter of YBCO along the c -axis ($c_{\text{YBCO}} = 11.68 \text{ \AA}$), such dislocations have a large energy associated with them—as the formation energy of a dislocation is proportional to the square of its

Burgers vector—essentially barring their formation. Alternatively, YBCO develops Y124 intergrowths as stacking faults parallel to the (001) plane by the insertion of an extra Cu-O atomic layer. As mentioned before, Y124's boundary may be considered as a partial dislocation with a Burgers vector $[0, 1/2, 1/6]$ [46], that is, a dislocation with both in- and out-of-plane components. Hence, as in other cubic and tetragonal perovskites [47], the appearance of Y124 intergrowths can be considered a mechanism by which the stress is relieved; an analogous situation to the nucleation of intergrowths at grain boundaries and Y_2BaCuO_5 -YBCO interfaces in melt-textured materials [48, 49].

In the particular case of metal-organic deposited YBCO films, Y124 planar defects are usually prevalent. In solution-derived nanocomposites, epitaxial YBCO nucleation and growth is delayed compared with nucleation and growth of the randomly distributed nanoparticles [9, 50]. Hence, stress is built up as YBCO encounters *obstacles*, such as randomly oriented nanoparticles [11, 13, 18, 51], during the growth process. On the other hand, in physical growth methods, such as pulsed laser deposition (PLD) and sputtering, both the YBCO and the secondary phases grow at the same time, and the interface between them is coherent or semicoherent. In this case, the elastic strain is mainly accommodated by the nanoparticles or the nanorods with misfit dislocations, interface distortions, and oxygen vacancies although limited to few unit cells [10, 15]. However, the appearance of Y124 intergrowths has also been reported when the mismatch or the concentration of secondary phases is high [8, 15, 16]. Therefore, by modifying the deposition technique one can ensure different microstructures, rendering dramatic changes in the flux-pinning mechanism: while films grown by PLD usually show directional effects in J_c , solution-derived composites exhibit a characteristic isotropic pinning behavior [9, 36, 52]. Regardless of the deposition technique, the presence of Y124 intergrowths within the YBCO films is highly desirable because they play an important role in vortex pinning, as their shape and size, as well as the strain generated around the associated partial dislocations at their boundaries, affect the flux-pinning and the critical current carried by the superconductor [9, 50, 53–56].

The larger amount of Y124 intergrowths and the presence of secondary phases within the nanocomposite films strongly affect another common defect in YBCO superconductors, twin boundaries (TB). Such defects appear to relieve the spontaneous strain that arises during the tetragonal-to-orthorhombic transition, which takes place during the last stage of the growth process, the oxygenation step [57]. In a defect-free environment, TBs can extend up to its critical twin-spacing, which is controlled by the film thickness and substrate constraints. In a 300 nm-thick YBCO film, the spacing between twins is around 100 nm [11, 58]. However, in the presence of Y124 defects the vertical TB coherence is broken. Figure 7.6a shows a Z-contrast image of a nanocomposite film, while Fig. 7.6b shows the ϵ_{xx} deformation tensor map ensuing from the {100} Bragg reflection. This deformation map has been generated using the Geometrical Phase Analysis (GPA) software, which is extremely useful for strain determination, as it is able to extract local displacements and rotations of atomic planes from the Fourier analysis of a high-resolution lattice image [59]. Here, [100] and [010] domains can be unambiguously distinguished

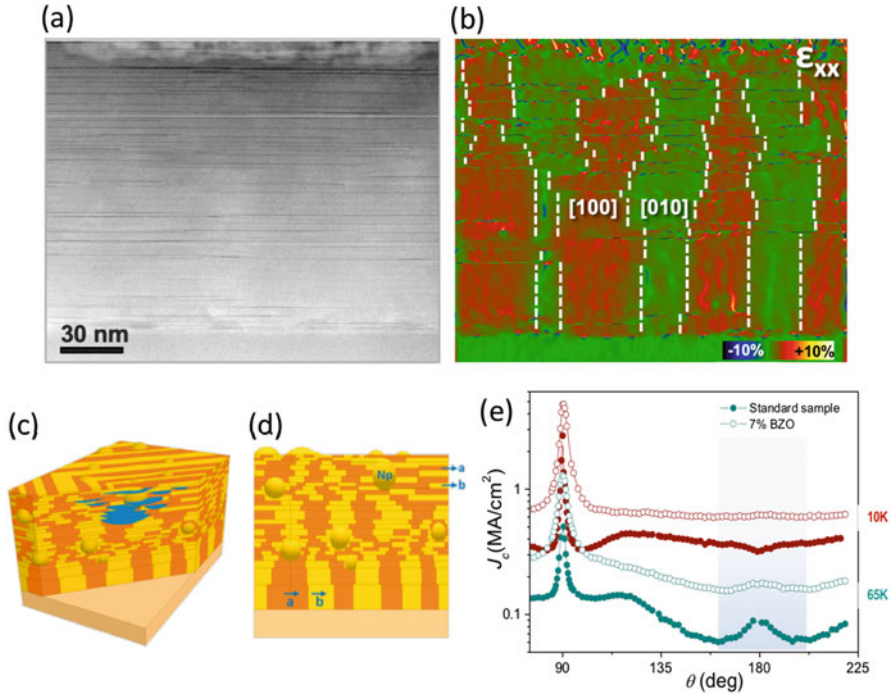


Fig. 7.6 (a) Low-magnification Z-contrast image of a YBCO-10% Y_2O_3 nanocomposite presenting a high density of Y124 defects, visible as dark stripes. Image acquired at 300 kV on the aberration-corrected FEI Titan. (b) ϵ_{xx} deformation map showing in colors (red and green) different deformation values, corresponding to the [100] and [010] twin domains. Notice that the twin coherence is broken along the film, thus denoting the strong structural interaction between both defects. (c, d) Sketches illustrating crystal twinning in highly faulted orthorhombic YBCO. Y124 intergrowths are shown in blue. (e) Angular dependence of J_c at 9 T for a standard YBCO film (closed symbols) and a nanocomposite (open symbols) at 10 K (red) and at 65 K (green). Adapted from [11]

by GPA due to the existing differences between a and b cell parameters in the orthorhombic phase of YBCO ($a = 0.382$ nm; $b = 0.388$ nm).

The higher density of defects produces a strong variation of the twin-spacing and a break in the twin boundary coherence; see the sketches in Fig. 7.6c, d. This scenario changes the understanding of TBs in nanocomposites, as they can act as pinning sites or as flux channels. The reduction of the TB vertical coherence has a relevant effect on precluding vortex channeling at low temperatures and thus avoiding a suppression of J_c for fields parallel to the c -axis ($\theta = 180^\circ$ in the image) [11, 58], see Fig. 7.6e.

The interaction between TBs and Y124 intergrowths is strain mediated, that is, the partial dislocation and its associated distortions constitute a barrier for propagation of the TB. This strain, as it changes the microstructure of the YBCO films, also transforms the pinning landscape of the nanocomposites. The localization

of the vortices' core at insulating regions (provided their dimension is in the range of the coherence length ξ) is not the only effective vortex-pinning mechanism; tensile strain can also quench the formation of Cooper pairs and constitute another effective pinning mechanism in high-temperature superconductors [17, 18, 60].

Although the combination of high-angle and low-angle ADF STEM images is an easy and straightforward method to visualize the nanoscale lattice deformations present in the YBCO matrix—that are associated to defects and nanoparticles—one needs to quantify the lattice deformation in order to infer the effectiveness of the partial dislocations associated to the Y124 intergrowths as a vortex-pinning site [17, 60], which can be done using GPA analysis. The Z-contrast image in Fig. 7.7a shows the presence of a Y124 intergrowth in an almost defect-free YBCO region, whereas Fig. 7.7c, d show the corresponding ε_{xx} and ε_{yy} deformation maps, respectively. The most evident lattice deformation is observed in the ε_{yy} map surrounding the partial dislocation core, which gradually vanishes away from the dislocation core, see Fig. 7.7d. On the other hand, the ε_{xx} map shows a $+1.4 \pm 1.1\%$ tensile deformation located right at the partial dislocation core, suggesting localized strain-induced pair suppression in YBCO, and thus constituting an effective vortex-pinning center [17]. The same occurs in Frank sessile dislocations, which are formed when a twin boundary crosses a Y124 intergrowth, as shown in Fig. 7.8a, b. The ε_{xx} GPA deformation map of the Z-contrast image shows two crystal domains, [010] domain in green and [100] domain in red, in addition to the compressive and tensile deformations around the dislocation core, signaled with an arrow. Since the Y124 structure involves the addition of an extra Cu-O chain and a structural shift of $1/2b_0$, a linear defect that separates the two crystal orientations must be present, this is a dislocation along the twin boundary plane, i.e., $\langle 100 \rangle_{\text{YBCO}}$ [13].

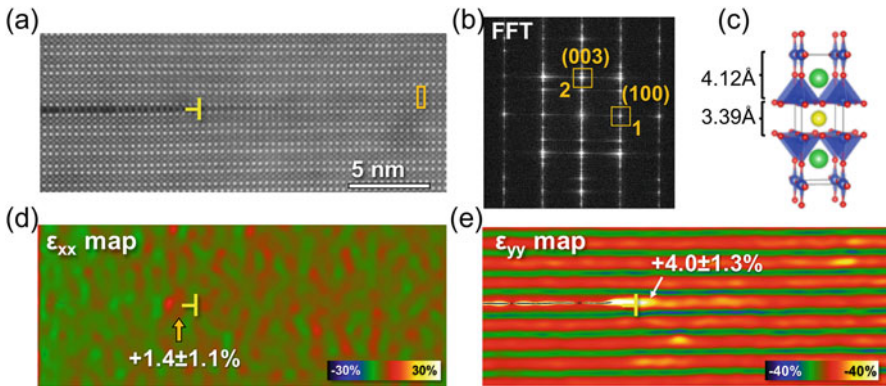


Fig. 7.7 (a) Z-contrast image of YBCO with a single isolated intergrowth. Image acquired at 300 kV on the aberration-corrected FEI Titan. (b) Fast Fourier Transform showing the Bragg reflections, {100} and {003}, used to generate the GPA deformation maps. (c, d) ε_{xx} and ε_{yy} deformation maps along $[100]_{\text{YBCO}}$ and $[001]_{\text{YBCO}}$ directions, respectively. The marked region in (a), the Z-contrast image is the reference lattice. (e) Sketch of the YBCO structure showing the two spacings that appear in the ε_{yy} deformation map. Adapted from [13]

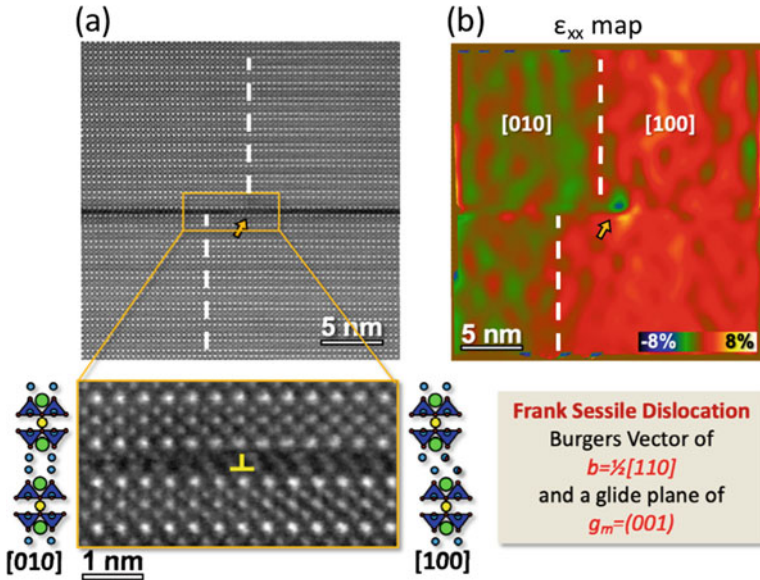


Fig. 7.8 (a, b) Show a Z-contrast image of an isolated Y124 intergrowth and its corresponding ϵ_{xx} GPA deformation map of the Z-contrast image. The two twin domains are shown in red and green colors. Image acquired at 300 kV on the aberration-corrected FEI Titan. The $\{100\}_{\text{YBCO}}$ Bragg reflections are used for computing the GPA map. Inset is a detailed image of the Frank sessile dislocation with a $1/2 [110]$ Burgers vector and a (001) glide plane located between the two CuO layers. The Y124 structure is illustrated in the image along $[100]$ and $[010]$ zone axes, where Green = Ba, Yellow = Y, Blue = Cu, and Red = O. The yellow symbol marks the position of the dislocation. Adapted from [13]

7.4 The Y124 Intergrowth: A Burst of Changes

As already mentioned, the presence of Y124 intergrowths is highly desirable because they play an important role in vortex pinning. However, it may be argued that the extra amount of Cu that would be needed for their formation would lead to a local Cu off-stoichiometry, as both the solution precursors and the targets (used in magnetron sputtering or pulsed laser deposition techniques) employed in YBCO synthesis have an exact 1:2:3 stoichiometry for Y, Ba, and Cu. The situation worsens in the case of YBCO nanocomposites, where the introduction of secondary phases within the layer may render a huge increase of Y124 intergrowths. For instance, this Cu off-stoichiometry could affect the critical temperature (T_c) of all the films that present a huge amount of these intergrowths, although, this detrimental effect has not been reported, being the $T_c \sim 90$ K in these defective films, which is similar to the pristine YBCO films. The reason, as it will be shown below, is that the system balances this deficiency of Cu by forming Cu and O vacancies buried within the very same intergrowth [12], thus preventing the stoichiometry catastrophe.

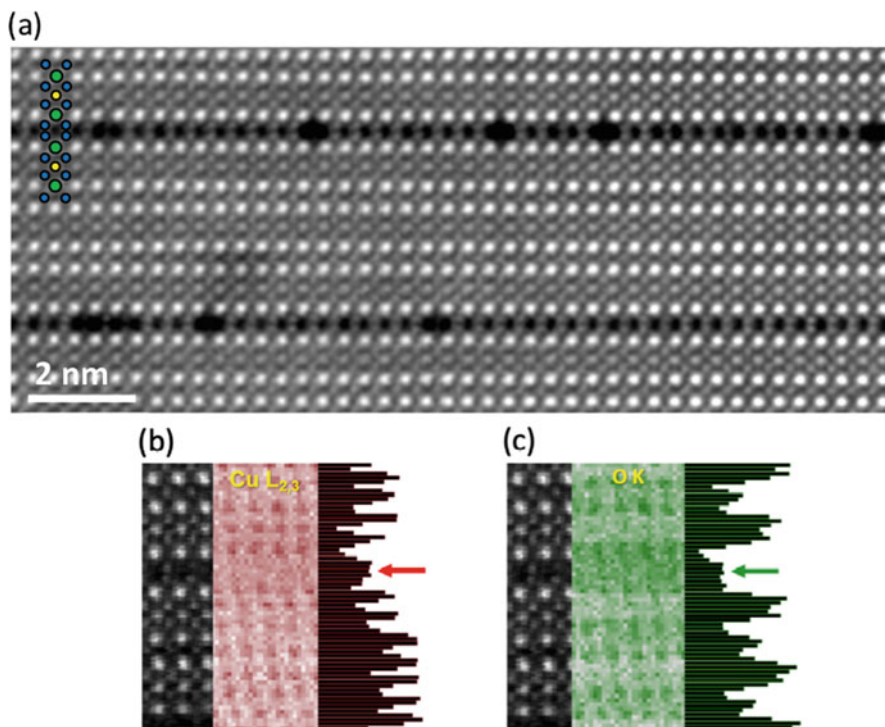


Fig. 7.9 (a) Z-contrast image of two Y124 intergrowths viewed along the [010] zone-axis direction. The Ba, Y, and Cu atomic columns are represented with green, yellow, and blue circles, respectively. Scale bar: 2 nm. Image acquired at 300 kV on the aberration-corrected FEI Titan. (b) Cu (red) and (c) O (green) EELS compositional maps. Each image displays, from left to right, the ADF simultaneous image, the EELS compositional map and the row-averaged EELS signal profile. The arrows point to the Y124 intergrowth position. Data acquired at 100 kV on the aberration-corrected Nion UltraSTEM. Adapted from [12]

Figure 7.9a shows a Z-contrast image of the YBCO phase with two Y124 intergrowth defects, each one viewed along the [010] zone-axis direction. The contrast within the double Cu-O chains randomly varies along the basal direction, with a lower brightness at some Cu columns. This lowering of intensity is ascribed to the presence of pairs of Cu vacancies (V_{Cu}) [12]. In Fig. 7.9b, c, the Cu and O EELS compositional maps are displayed as red and green color maps, respectively. The vertical profiles correspond to the relative atomic composition (Cu and O) depth-profiles, which are obtained by summing the intensities of each row in the map. In the double-chain (marked by red and green arrows), both the Cu and O signals are observed to be lower than in the single-chain positions, pointing towards the presence of complex Cu-O vacancies.

DFT calculations allowed for estimating the stability of different vacancy configurations by comparing their formation energies at 0 K. A supercell structure

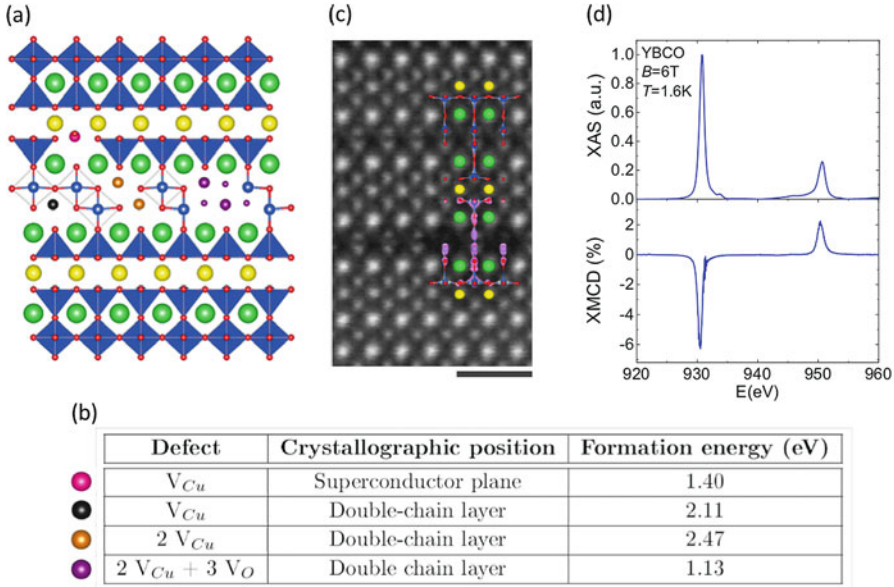


Fig. 7.10 (a) Illustration of the Y248 crystal structure. The pink, orange, black, and magenta circles indicate some of the crystallographic sites where single V_{Cu} and clusters of $V_{Cu} + V_O$ have been tested using DFT calculations. The Ba, Y, Cu, and O atomic columns are represented with green, yellow, blue, and red circles, respectively. (b) Formation energy associated to the specific vacancy configuration represented in (a) at 0 K. (c) Z-contrast image with the isosurface plot of the spin density showing the magnetic moment associated with a $2V_{Cu} + 3V_O$ defect in Y248. Image acquired at 200 kV on the aberration-corrected Nion UltraSTEM. (d) Cu $L_{2,3}$ edge (top) background-subtracted XAS and (bottom) XMCD spectra measured at 6 T, 1.6 K in normal incidence ($\theta = 0^\circ$) for the standard YBCO thin film in Total Electron Yield (TEY) mode. Scale bar: 1 nm. Adapted from [12]

composed by a $Y_2Ba_4Cu_8O_{16}$ (Y248) stoichiometry containing Cu-O double-chain layers instead of Cu-O single chains was used [12], which is represented in Fig. 7.10a. The formation energy of most relevant defects obtained from the DFT calculations is summarized in the table of Fig. 7.10b. The most favorable vacancy configuration—that also matches with the EELS experimental data—corresponds to the case where two Cu vacancies are accompanied with three oxygen vacancies ($2V_{Cu} + 3V_O$, purple in Fig. 7.8a), with one O vacancy located in the upper Cu-O chain and two in the lower one. DFT also allowed insights into the effect of these complex defects on the electronic and magnetic properties of the system in the metallic phase. The most striking effect is the fact that the O-decorated Cu vacancies give rise to a finite magnetic moment of $\approx 2.2 \mu_B$ per $2V_{Cu} + 3V_O$ defect cluster [12]. Figure 7.10c shows an isosurface plot of the spin density around one such defect cluster. Notice that the magnetization extends to the neighboring CuO_2 planes, which implies that the defect structure also provides an extra vortex-pinning contribution, since the magnetic vortices formed by flux lines should find

it favorable to go through this non-superconducting and magnetic defect with nanoscale dimensions.

X-ray magnetic circular dichroism (XMCD) at the Cu $L_{2,3}$ edge was used to experimentally prove the existence of the predicted magnetic moment associated with these complex defects. XMCD experiments were performed in Total Electron Yield (TEY) detection mode on two samples, a pristine YBCO film and a YBCO + BYTO nanocomposite thin film, both of which exhibited a high Y124 intergrowth concentration within the superficial TEY probing depth (~ 6 nm). XMCD is an element-sensitive technique which involves recording the difference between the X-ray absorption for left- and right-polarized photons. If the Cu-XMCD difference is non-zero, it suggests the presence of magnetic moments on the probed atoms, which in this case is Cu. This is demonstrated in Fig. 7.10d, which shows a dichroic signal obtained in a YBCO film measured at 6 T and at a temperature of 1.6 K. Both samples, the pristine YBCO film and the YBCO + BYTO nanocomposite, displayed qualitatively similar Cu $L_{2,3}$ edge fine structure and dichroic spectra. The XMCD as a function of the magnetic field dependence displayed a superparamagnetic behavior even below T_c , which was assigned to the presence of the complex $2V_{Cu} + 3V_O$ defects with an associated cluster ferromagnetic moment [12]. The same superparamagnetic signal has been detected in hybrid YBCO nanocomposites thin films, allowing to propose a model in which the magnetism of Cu atoms in superconducting YBCO films can be explained in terms of a superparamagnetic behavior of isolated ferromagnetic clusters, even below T_c [12, 61]. The fact that these defect clusters are found in large numbers in YBCO nanocomposites, which show at the same time an enormous enhancement of vortex-pinning efficiency, makes one wonder if this novel behavior plays a role in efficiently pinning vortices. Thus, they are an excellent playground to investigate the interaction between superconducting vortices and ferromagnetic clusters at low temperatures.

DFT calculations revealed that the $2V_{Cu} + 3V_O$ defect is more stable under low oxygen pressures, precisely the conditions under which the YBCO films are grown [12]. Therefore, one would expect that the single crystals, which are grown under higher oxygen pressures, did not present the most favorable conditions for the formation of the Cu divacancies. However, STEM analyses of a single crystal revealed the existence of both Cu and O vacancies within the Y124 intergrowths. The low-magnification image shown in Fig. 7.11a evidences that the presence of Y124 intergrowths is restricted to only a few nanometers below the surface of the single crystal, while the high magnification image shown in Fig. 7.11b demonstrates the existence of Cu divacancies within the intergrowths. Interestingly, the Cu-XMCD measurements in TEY (surface) mode from the very same sample presented a robust dichroic signal of about 5%. These results prove that whenever the Y124 intergrowths are present in YBCO there are Cu divacancies buried in them with an associated magnetic moment.

Furthermore, in order to attest the DFT-predicted structure of the $2V_{Cu} + 3V_O$ defects, one can use the ABF imaging mode, which is able to probe all the atomic sub-lattices. Figure 7.12a, b, respectively, show the Z-contrast and the ABF images

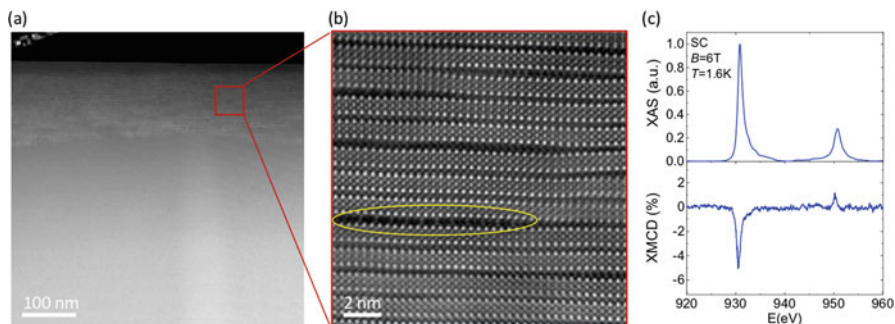


Fig. 7.11 (a) Z-contrast image of a YBCO single crystal. (b) Higher magnification Z-contrast image of the surface of the crystal showing a large concentration of Y124 intergrowths. A region with a visible concentration of Cu vacancies is marked with a yellow circle. Data acquired at 200 kV on the aberration-corrected Nion UltraSTEM. (c) Cu $L_{2,3}$ edge (top) background-subtracted XAS and (bottom) XMCD spectra measured at 6 T, 1.6 K in normal incidence ($\theta = 0^\circ$) for the YBCO single crystal obtained under TEY mode

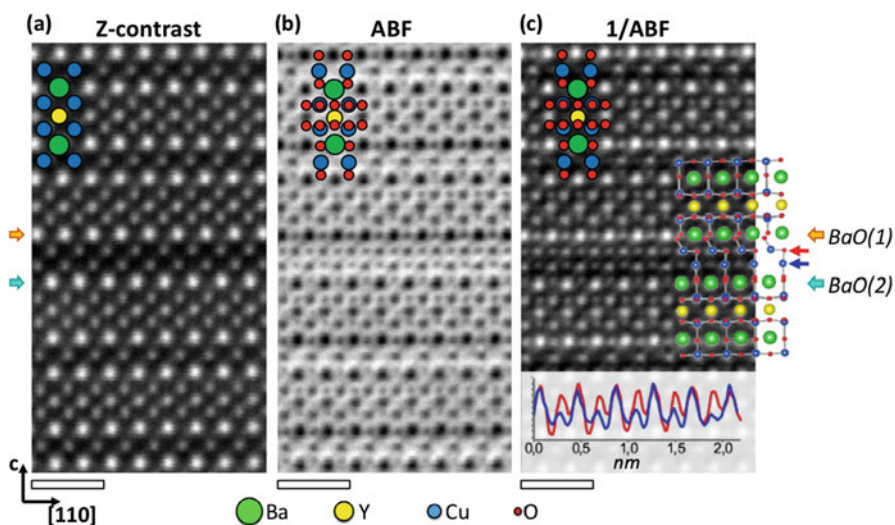


Fig. 7.12 (a) Z-contrast, (b) ABF, and (c) contrast-inverted ABF images of an isolated Y124 intergrowth viewed along the $[100]$ zone-axis direction. The DFT-simulated structure is superimposed in (c). The inset shows two horizontal intensity profiles measured along the upper (red) and lower (blue) Cu-O double-chains. Although not shown, the substrate is located downwards and defines what is called upper and lower Cu-O chains, with the lower chain being closer to the substrate. The Ba, Y, Cu, and O atomic columns are represented with green, yellow, blue, and red circles, respectively. Scale bars: 0.5 nm. Data acquired at 200 kV on the aberration-corrected Nion UltraSTEM

of the YBCO lattice with an isolated Y124 intergrowth along the $[100]$ zone axis. The inverted ABF image, Fig. 7.12c, unveils clearly the oxygen sub-lattice and shows a perfect match with the DFT-predicted structure. In particular, the experimental image shows that the relative O content of both Cu-O planes of the Y124 intergrowth is different. The lower Cu-O chain (blue arrow in Fig. 7.12c) contains more O vacancies, therefore, has a lower O atomic column intensity, as shown in the horizontal trace of the intensity profiles along the two Cu-O chains of the intergrowth, see inset of Fig. 7.12c. Remarkably, this uneven distribution of oxygen vacancies is general, as the lower Cu-O plane of the intergrowth (the one closer to the substrate, which is located at the bottom of the image, although not shown) always presents a lower content of oxygen. This suggests that the distribution of oxygen vacancies is dictated by kinetic effects, during the layer-by-layer bottom-to-top growth process. In addition, a careful inspection of the Ba-O plane right under the double Cu-O chain shows that some of the apical oxygens, those in the O(2) site, are slightly shifted upwards as well, resulting in a rod instead of a round atomic column in the contrast-inverted ABF image, which was also predicted by DFT calculations; see the sketched structure of the inset in Fig. 7.12c.

Yet, Y124 intergrowths hold in store more surprises, as subtle structural changes occur around them. Figure 7.13a–c show a high-resolution Z-contrast image of the YBCO matrix with two Y124 intergrowths, the out-of-plane spacings map between the heaviest cations (Y and Ba) and the averaged profile across the intergrowths, respectively. Notice that the profile distinguishes three different spacings: the Y–Ba, the Ba–Y, and the Ba–Ba spacings. These results show that close to the intergrowth the Ba–Y spacing is smaller than the Y–Ba spacing, as represented in Fig. 7.13d;

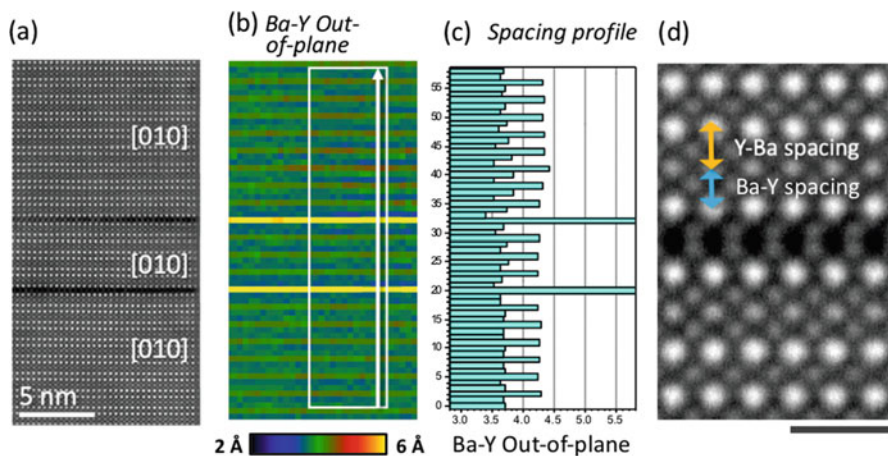


Fig. 7.13 (a) Atomic resolution image of YBCO lattice with two Y124 intergrowths imaged along the $[010]$ orientation. (b) Y–Ba, Ba–Y, and Ba–Ba out-of-plane spacings calculated from (a). (c) Y–Ba, Ba–Y, and Ba–Ba averaged spacing profile of (b). (d) higher resolution Z-contrast image of YBCO showing the Y–Ba and Ba–Y spacings. Scale bar: 1 nm. Data acquired at 300 kV on the aberration-corrected FEI Titan

whereas farther from the intergrowth (>5-unit cells) the spacings become equal and recover the expected value for defect-free YBCO.

What is the cause of such striking result? ABF imaging of the YBCO matrix in the presence of a Y124 intergrowth, as shown in Fig. 7.12, gives the answer to this question. In the inverted ABF image, see Fig. 7.12c, the O columns located within the BaO(1) plane that is present above the fault (orange arrow) appear brighter than those belonging to the lower BaO(2) plane (blue arrow). It should be noted that the difference in contrast between the BaO(1) and BaO(2) planes evidences that the latter contain oxygen vacancies, and also that of the two BaO planes that are present within the YBCO unit cell, the BaO(1) one is always closer to the film's surface. Although anticipated in previous results [62–65], this constitutes the first direct experimental observation of apical oxygen vacancies ($V_{\text{O}}^{\text{BaO}}$) in the BaO plane.

The presence of $V_{\text{O}}^{\text{BaO}}$ is linked to the Y124 intergrowths as these vacancies are absent farther from the intergrowths. Independent of the growth process used, and even for the YBCO single crystals, $V_{\text{O}}^{\text{BaO}}$ oxygen vacancies appear in every other Ba-O plane close to the intergrowths, which rules out the origin of these vacancies to the strain induced due to lattice mismatch of YBCO with a substrate. Instead, their existence seems to be related to the local strain generated when an extra Cu-O plane is added once a YBCO intergrowth is generated [to be published].

The stability of the $V_{\text{O}}^{\text{BaO}}$ has also been studied by DFT calculations. The plot in Fig. 7.14 shows the formation energy of apical or planar oxygen vacancies for varying concentrations, relative to the energies of the well-known $V_{\text{O}}^{\text{CuO}}$. $V_{\text{O}}^{\text{CuO}}$ is more favorable at high vacancy concentrations because multiple vacancies can order along the chains, which stabilizes them. However, in the optimal doping region,

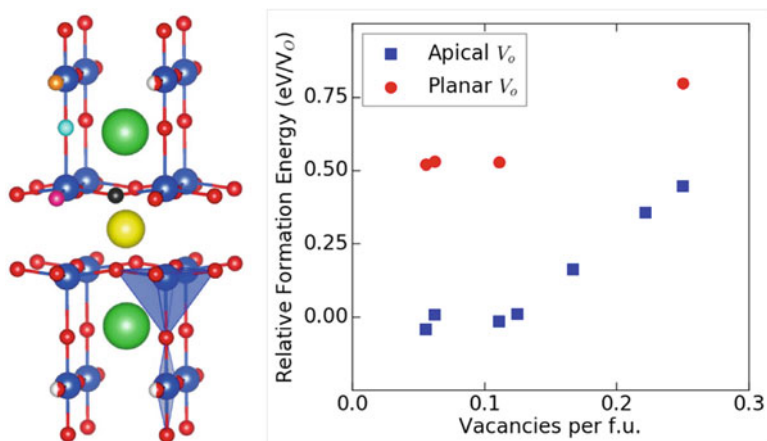


Fig. 7.14 Left panel, sketch of the YBCO unit cell with the position of the oxygen vacancies painted in different colors. Right panel, a plot of the formation energy of oxygen vacancies in different crystallographic sites as a function of vacancy concentration per formula unit (f.u.). The energies are calculated relative to the most stable ordering of $V_{\text{O}}^{\text{CuO}}$ at that concentration

V_{O}^{BaO} and V_{O}^{CuO} have nearly identical formation energies, indicating that they are equally likely to form. The formation energy increases when the V_O is placed in the superconducting planes, indicating that planar vacancies should not be present in large numbers. These theoretical calculations are in excellent agreement with the experimental observations.

Obviously, the presence of V_{O}^{BaO} will trigger structural distortions that can also be identified using the ABF imaging mode. Figure 7.15a shows a contrast-inverted ABF image of the YBCO lattice surrounding two Y124 intergrowths. A higher magnification contrast-inverted ABF image, shown in Fig. 7.15b, unveils, at first glance, the structural changes that take place in the oxygen sub-lattice. The oxygen atoms of the superconducting planes are shifted towards the Y cation in the undistorted structure, forming a rippling pattern with their neighboring Cu cations. This rippling is clearly identified in the superconducting plane that is farther away from the Ba-O plane containing oxygen vacancies. However, this rippling almost disappears in the upper superconducting plane. In addition, the apical oxygen atoms located in the Ba-O planes containing oxygen vacancies are shifted upwards, and as a result, the spacing between the Cu lying in the superconducting plane and its nearest apical oxygen (δ_{ap}) is greater than the lower one. These distortions modify the Cu-O bondings, in particular the in-plane and the apical oxygen height of the

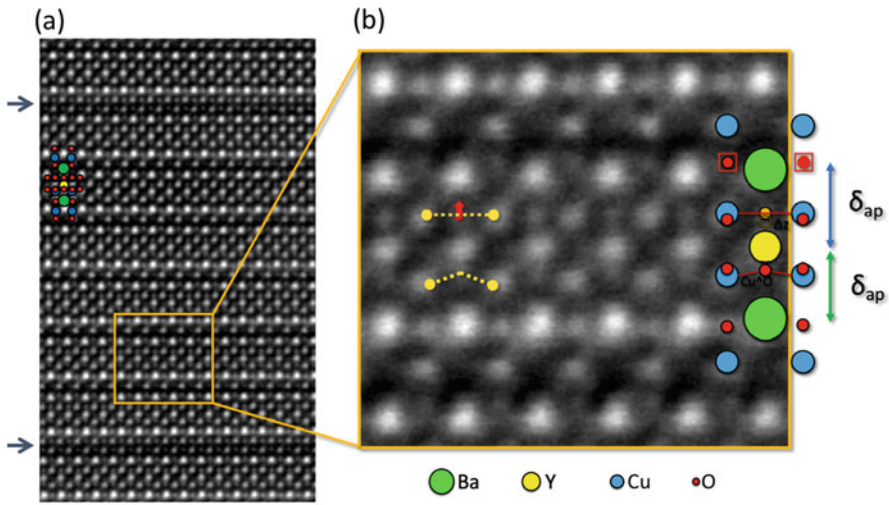


Fig. 7.15 (a) High-resolution contrast-inverted ABF image of a region in a YBCO thin film containing two Y124 intergrowths, signaled with blue arrows. Scale bar: 1 nm. The orange rectangular area is magnified in (b). The Ba, Y, Cu, and O atomic columns are represented with green, yellow, blue, and red circles, respectively. The change in the Cu–O–Cu angles is marked in yellow. The red arrow signals the upward shift of the apical oxygen. Data acquired at 200 kV on the aberration-corrected Nion UltraSTEM

superconducting planes, and will affect the electronic structure of the YBCO, and thus a detailed theoretical study of the electronic states locally around these defects is required.

7.5 Summary

Abraham Lincoln once said, “It has been my experience that folks who have no vices have very few virtues.” This bit of wisdom applies equally well to defects in materials. Defects are generally seen as detrimental to their functionality and applicability, however, in some complex oxides, they present an opportunity to enhance particular properties. A paradigmatic example is the high-temperature superconductor YBCO, in which defects play an essential role in pinning quantized magnetic vortices and preventing energy losses. As not all defects are effective, it is necessary to have a high degree of understanding of their structure, chemistry as well as of how defects behave and interact within the YBCO matrix. This is achieved by a combination of microscopic experiments and first-principles calculations.

In this chapter, it has been shown that by using a combination of aberration-corrected scanning transmission electron microscopy (STEM), electron energy loss spectroscopy (EELS), density-functional-theory (DFT) calculations and X-ray magnetic circular dichroism (XMCD), one can shed light on the complex defect landscape of YBCO thin films and nanocomposites and unveil the presence of previously disregarded defects embedded in YBCO, as well as measure their effect on the atomic spacings, hence quantifying strain at the unit-cell level, allowing the description of peculiar electronic and magnetic properties.

Acknowledgements Authors acknowledge the MICIN (NANOSELECT, DUARFS MAT2017-83468-R and MAT2014-51778-C2-1-R), Generalitat de Catalunya (2014SGR 753 and Xarmae), and the EU (EU-FP7 NMP-LA-2012-280432 EUROTAPES project). They also acknowledge financial support from the Spanish Ministry of Economy, Industry and Competitiveness, through the “Severo Ochoa” Programme for Centres of Excellence in R&D (SEV-2015-0496). STEM imaging and analysis at 200 kV was sponsored by the U.S. Department of Energy, Office of Science, Basic Energy Sciences, Materials Sciences and Engineering Division, and STEM imaging at 100 kV was conducted at the Center for Nanophase Materials Sciences, which is a DOE Office of Science User Facility. STEM imaging and analysis at 300 kV was conducted in the Laboratorio de Microscopías Avanzadas (LMA) at Instituto de Nanociencia de Aragón (INA) at the University of Zaragoza. J.G. also acknowledges the Ramón y Cajal program (RYC-2012-11709). The work at Washington University (S.T.H. and R.M.) was supported by the National Science Foundation (NSF) grant number DMR-1806147. This work used the computational resources of the Extreme Science and Engineering Discovery Environment (XSEDE), which is supported by National Science Foundation grants ACI-1053575 and ACI-1548562.

The authors are grateful to all the collaborators who made this work possible over the years, especially to Teresa Puig, Xavier Obradors, Mariona Coll, Anna Palau, Anna Llordes, Juan Salafranca, Maria Varela, Juan Carlos Idrobo, Cesar Magen, Pablo Cayado, S. Manuel Valvidares, Pierluigi Gargiani, Eric Pellegrin, Javier Herrero-Martin, Wolfgang Windl, Matt Chisholm, Sokrates T. Pantelides, and Stephen J. Pennycook.

References

1. D. Dimos, P. Chaudhari, J. Mannhart, *Phys. Rev. B* **41**, 4038 (1990)
2. M.P. Paranthaman, T. Izumi, *MRS Bull.* **29**, 533 (2004)
3. X. Song, Z. Chen, S.-I. Kim, D.M. Feldmann, D. Larbalestier, J. Reeves, Y. Xie, V. Selvamanickam, *Appl. Phys. Lett.* **88**, 212508 (2006)
4. Y. Yamada, K. Takahashi, H. Kobayashi, M. Konishi, T. Watanabe, A. Ibi, T. Muroga, S. Miyata, T. Kato, T. Hirayama, Y. Shiohara, *Appl. Phys. Lett.* **87**, 132502 (2005)
5. S. Kang, A. Goyal, J. Li, A.A. Gapud, P.M. Martin, L. Heatherly, J.R. Thompson, D.K. Christen, F.A. List, M. Paranthaman, D.F. Lee, *Science* **311**, 1911 (2006)
6. T. Haugan, P.N. Barnes, R. Wheeler, F. Meisenkothen, M. Sumption, *Nature* **430**, 867 (2004)
7. J.L. MacManus-Driscoll, S.R. Foltyn, Q.X. Jia, H. Wang, A. Serquis, L. Civale, B. Maiorov, M.E. Hawley, M.P. Maley, D.E. Peterson, *Nat. Mater.* **3**, 439 (2004)
8. P. Mele, R. Guzman, J. Gazquez, T. Puig, X. Obradors, S. Saini, Y. Yoshida, M. Mukaida, A. Ichinose, K. Matsumoto, M. Idries Adam, *Supercond. Sci. Technol.* **28**, 024002 (2015)
9. A. Llordés, A. Palau, J. Gázquez, M. Coll, *Nat. Mater.* **11**, 329 (2012)
10. C. Cantoni, Y. Gao, S.H. Wee, E.D. Specht, J. Gazquez, J. Meng, S.J. Pennycook, A. Goyal, *ACS Nano* **5**, 4783 (2011)
11. R. Guzman, J. Gazquez, V. Rouco, A. Palau, C. Magen, M. Varela, J. Arbiol, X. Obradors, T. Puig, *Appl. Phys. Lett.* **102**, 081906 (2013)
12. J. Gazquez, R. Guzman, R. Mishra, E. Bartolomé, J. Salafranca, C. Magén, M. Varela, M. Coll, A. Palau, S.M. Valvidares, P. Gargiani, E. Pellegrin, J. Herrero-Martin, S.J. Pennycook, S.T. Pantelides, T. Puig, X. Obradors, *Adv. Sci.* **3**, 1500295 (2016)
13. R. Guzman, J. Gazquez, B. Mundet, M. Coll, X. Obradors, T. Puig, *Phys. Rev. Mater.* **1**, 024801 (2017)
14. A.K. Jha, K. Matsumoto, T. Horide, S. Saini, P. Mele, A. Ichinose, Y. Yoshida, S. Awaji, *J. Appl. Phys.* **122**, 093905 (2017)
15. T. Horide, F. Kametani, S. Yoshioka, T. Kitamura, K. Matsumoto, *ACS Nano* **11**, 1780 (2017)
16. T. Maeda, K. Kaneko, K. Yamada, A. Roy, Y. Sato, R. Teranishi, T. Kato, T. Izumi, Y. Shiohara, *Ultramicroscopy* **176**, 151 (2017)
17. G. Deutscher, *Appl. Phys. Lett.* **96**, 1 (2010)
18. A. Llordés, A. Palau, J. Gázquez, M. Coll, R. Vlad, A. Pomar, J. Arbiol, R. Guzmán, S. Ye, V. Rouco, F. Sandiumenge, S. Ricart, T. Puig, M. Varela, D. Chateigner, J. Vanacken, J. Gutiérrez, V. Moshchalkov, G. Deutscher, C. Magen, X. Obradors, *Nat. Mater.* **11**, 329 (2012)
19. S.J. Pennycook, P.D. Nellist, *Scanning Transmission Electron Microscopy* (Springer, New York, 2011)
20. S.J. Pennycook, D.E. Jesson, *Ultramicroscopy* **37**, 14 (1991)
21. P.D. Nellist, S.J. Pennycook, *Ultramicroscopy* **78**, 111 (1999)
22. P.D. Nellist, S.J. Pennycook, *Science* **274**, 413 (1996)
23. A.Y. Borisevich, A.R. Lupini, S.J. Pennycook, *Proc. Natl. Acad. Sci. U. S. A.* **103**, 3044 (2006)
24. R. Ishikawa, E. Okunishi, H. Sawada, Y. Kondo, F. Hosokawa, E. Abe, *Nat. Mater.* **10**, 278 (2011)
25. W.M. Temmerman, H. Winter, Z. Szotek, A. Svane, *Phys. Rev. Lett.* **86**, 2435 (2001)
26. R. Liang, D.A. Bonn, W.N. Hardy, *Phys. Rev. B* **73**, 180505 (2006)
27. N.D. Browning, J. Yuan, L.M. Brown, *Phys. C Supercond.* **202**, 12 (1992)
28. N. Gauquelin, D.G. Hawthorn, G.A. Sawatzky, R.X. Liang, D.A. Bonn, W.N. Hardy, G.A. Botton, *Nat. Commun.* **5**, 4275 (2014)
29. D.G. Hawthorn, K.M. Shen, J. Geck, D.C. Peets, H. Wadati, J. Okamoto, S.-W. Huang, D.J. Huang, H.-J. Lin, J.D. Denlinger, R. Liang, D.A. Bonn, W.N. Hardy, G.A. Sawatzky, *Phys. Rev. B* **84**, 075125 (2011)
30. M. Gioni, J.F. van Acker, M.T. Czyżyk, J.C. Fuggle, *Phys. Rev. B* **45**, 3309 (1992)

31. P. Cayado, B. Mundet, H. Eloussifi, F. Vallès, M. Coll, S. Ricart, J. Gázquez, A. Palau, P. Roura, J. Farjas, T. Puig, X. Obradors, *Supercond. Sci. Technol.* **30**, 1361 (2017)
32. S.H. Wee, Y.L. Zuev, C. Cantoni, A. Goyal, *Sci. Rep.* **3**, 2310 (2013)
33. A.A. Gapud, D. Kumar, S.K. Viswanathan, C. Cantoni, M. Varela, J. Biade, S.J. Pennycook, D.K. Christen, *Supercond. Sci. Technol.* **18**, 1502 (2005)
34. J. Gutiérrez, A. Lordés, J. Gázquez, M. Gibert, N. Romà, S. Ricart, A. Pomar, F. Sandiumenge, N. Mestres, T. Puig, X. Obradors, *Nat. Mater.* **6**, 1893 (2007)
35. X. Obradors, T. Puig, S. Ricart, M. Coll, J. Gázquez, A. Palau, X. Granados, *Supercond. Sci. Technol.* **25**, 123001 (2012)
36. K. Matsumoto, P. Mele, *Supercond. Sci. Technol.* **23**, 14001 (2010)
37. P. Mele, K. Matsumoto, T. Horide, A. Ichinose, M. Mukaida, Y. Yoshida, S. Horii, R. Kita, *Supercond. Sci. Technol.* **21**, 015019 (2008)
38. T. Horide, N. Sakamoto, A. Ichinose, K. Otsubo, T. Kitamura, K. Matsumoto, *Supercond. Sci. Technol.* **29**, 105010 (2016)
39. D.M. Feldmann, T.G. Holesinger, B. Maiorov, S.R. Foltyn, J.Y. Coulter, I. Apodaca, *Supercond. Sci. Technol.* **23**, 095004 (2010)
40. M. Coll, S. Ye, V. Rouco, A. Palau, R. Guzman, J. Gázquez, J. Arbiol, H. Suo, T. Puig, X. Obradors, *Supercond. Sci. Technol.* **26**, 015001 (2013)
41. D.A. Muller, N. Nakagawa, A. Ohtomo, J.L. Grazul, H.Y. Hwang, **430**, 657 (2004)
42. P.J. Phillips, M. De Graef, L. Kovarik, A. Agrawal, W. Windl, M.J. Mills, *Ultramicroscopy* **116**, 47 (2012)
43. H.W. Zandbergen, R. Gronsky, G. Thomas, *Phys. Status Solidi* **105**, 207 (1988)
44. H.W. Zandbergen, R. Gronsky, K. Wang, G. Thomas, *Nature* **331**, 596 (1988)
45. J. Rabier, P.D. Tall, M.F. Denanot, *Philos. Mag. A* **67**, 1021 (1993)
46. J. Taftø, M. Suenaga, R.L. Sabatini, *Appl. Phys. Lett.* **52**, 667 (1988)
47. P. Hirel, P. Marton, M. Mrovec, C. Elsässer, *Acta Mater.* **58**, 6072 (2010)
48. F. Sandiumenge, T. Puig, J. Rabier, J. Plain, X. Obradors, *Adv. Mater.* **12**, 375 (2000)
49. F. Sandiumenge, J. Rabier, *Studies of High Temperature Superconductors* (Nova Science, Narlikar, 1999)
50. T. Puig, J. Gutiérrez, A. Pomar, A. Lordés, J. Gázquez, S. Ricart, F. Sandiumenge, X. Obradors, *Supercond. Sci. Technol.* **21**, 34008 (2008)
51. J.A. Xia, N.J. Long, N.M. Strickland, P. Hoefakker, E.F. Talantsev, X. Li, W. Zhang, T. Kodenkandath, Y. Huang, M.W. Rupich, *Supercond. Sci. Technol.* **20**, 880 (2007)
52. A. Goyal, S. Kang, K.J. Leonard, P.M. Martin, A.A. Gapud, M. Varela, M. Paranthaman, A.O. Ijaluola, E.D. Specht, J.R. Thompson, D.K. Christen, S.J. Pennycook, F.A. List, *Supercond. Sci. Technol.* **18**, 1533 (2005)
53. T.G. Holesinger, L. Civale, B. Maiorov, D.M. Feldmann, J.Y. Coulter, D.J. Miller, V.A. Maroni, Z. Chen, D.C. Larbalestier, R. Feenstra, X. Li, Y. Huang, T. Kodenkandath, W. Zhang, M.W. Rupich, A.P. Malozemoff, *Adv. Mater.* **20**, 391 (2008)
54. H. Yamasaki, K. Ohki, I. Yamaguchi, M. Sohma, W. Kondo, H. Matsui, T. Manabe, T. Kumagai, *Supercond. Sci. Technol.* **23**, 105004 (2010)
55. E.D. Specht, A. Goyal, J. Li, P.M. Martin, X. Li, M.W. Rupich, *Appl. Phys. Lett.* **89**, 2006 (2006)
56. F. Vallès, A. Palau, V. Rouco, B. Mundet, X. Obradors, T. Puig, *Sci. Rep.* **8**, 5924 (2018)
57. C.J. Jou, J. Washburn, *J. Mater. Res.* **4**, 795 (1989)
58. V. Rouco, A. Palau, R. Guzman, J. Gázquez, M. Coll, X. Obradors, T. Puig, *Supercond. Sci. Technol.* **27**, 125009 (2014)
59. M.J.J. Hÿtch, E. Snoeck, R. Kilaas, *Ultramicroscopy* **74**, 131 (1998)
60. G. Deutscher, *J. Appl. Phys.* **111**, 112603 (2012)
61. E. Bartolomé, P. Cayado, E. Solano, C. Mocuta, S. Ricart, B. Mundet, M. Coll, J. Gázquez, A. Meledin, G. van Tendeloo, S.M. Valvidares, J. Herrero-Martín, P. Gargiani, E. Pellegrin, C. Magén, T. Puig, X. Obradors, *Adv. Electron. Mater.* **3**, 1700037 (2017)

62. J.C. Cheang Wong, C. Ortega, J. Siejka, I. Trimaille, A. Sacuto, L.M. Mercandalli, F. Mayca, *J. Alloys Compd.* **195**, 675 (1993)
63. A.P. Shapovalov, Y.M. Boguslavskij, A.I. Ruban, G.G. Gridneva, V.S. Melnikov, N.P. Pshentsova, *Supercond. Sci. Technol.* **5**, 283 (1992)
64. J.D. Jorgensen, M.A. Beno, D.G. Hinks, L. Soderholm, K.J. Volin, R.L. Hitterman, J.D. Grace, I.K. Schuller, C.U. Segre, K. Zhang, M.S. Kleefisch, *Phys. Rev. B* **36**, 3608 (1987)
65. J.D. Jorgensen, H. Shaked, D.G. Hinks, B. Dabrowski, B.W. Veal, A.P. Paulikas, L.J. Nowicki, G.W. Crabtree, W.K. Kwok, L.H. Nunez, H. Claus, *Phys. C Supercond.* **578**, 153–155 (1988)